High-Performance Rh2P Electrocatalyst for Efficient Water Splitting

Haohong Duan,[†,‡,∇] Dongguo Li,[§,∇] Yan Tang,[∥,∇] Yang He,[⊥] Shufang Ji,[†] Rongyue Wang,[§] Haifeng Lv,[§] Pietro P. Lopes,[§] Arvydas P. Paulikas,[§] Haoyi Li,[∥] Scott X. Mao,[⊥] Chongmin Wang,[#] Nenad M. Markovic,[§] Jun Li,*[∥] Vojislav R. Stamenkovic,*[§] and Yadong Li*[†]

†Department of Chemistry and Collaborative Innovation Center for Nanomaterial Science and Engineering, Tsinghua University, Beijing 100084, China

‡Chemistry Research Laboratory, Department of Chemistry, University of Oxford, 12 Mansfield Road, Oxford OX1 3TA, U.K.

§Materials Science Divisions, Argonne National Laboratory, Lemont, Illinois 60439, United States

∥Department of Chemistry and Key Laboratory of Organic Optoelectronics & Molecular Engineering of Ministry of Education, Tsinghua University, Beijing 100084, China

⊥Department of Mechanical Engineering and Materials Science, University of Pittsburgh, Pittsburgh, Pennsylvania 15261, United States

#Environmental Molecular Sciences Laboratory, Pacific Northwest National Laboratory, Richland, Washington 99352, United States

Ⓢ Supporting Information

ABSTRACT: The search for active, stable, and cost-efficient electrocatalysts for hydrogen production via water splitting could make a substantial impact on energy technologies that do not rely on fossil fuels. Here we report the synthesis of rhodium phosphide electrocatalyst with low metal loading in the form of nanocubes (NCs) dispersed in high-surface-area carbon (Rh_2P/C) by a facile solvo-thermal approach. The Rh_2P/C NCs exhibit remarkable performance for hydrogen evolution reaction and oxygen evolution reaction compared to Rh/C and Pt/C catalysts. The atomic structure of the Rh_2P NCs was directly observed by annular dark-field scanning transmission electron microscopy, which revealed a phosphorus-rich outermost atomic layer. Combined experimental and computational studies suggest that surface phosphorus plays a crucial role in determining the robust catalyst properties.
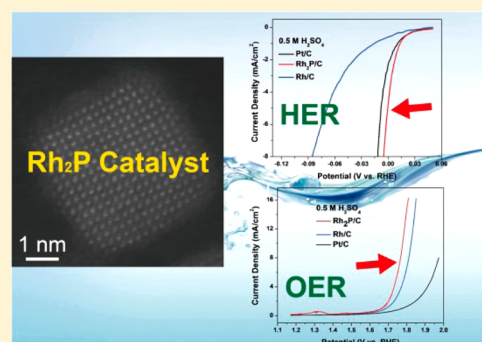
INTRODUCTION

Hydrogen fuel is a clean and abundant energy resource that could replace fossil fuels in the future.[1−3] Electrolysis of water, a sustainable approach for hydrogen production, requires an effective electrocatalyst for both the hydrogen evolution reaction (HER) and oxygen evolution reaction (OER).[4] While platinum is the conventional HER catalyst of choice due to its having the highest exchange current density and a low Tafel slope,[5] the high price limits its electrochemical applications, including use in fuel cells and electrolyzers.[4,6,7] Despite intensive research efforts toward the development of active, acid-stable, and low-cost HER catalysts in the past decade,[8] only a few examples of Pt-based catalysts with modified structure could exceed the HER activity in acidic environments when compared to the state-of-the-art commercial Pt/C.[9,10] Consequently, development of an active and affordable Pt-free catalyst remains a challenging task.

Transition-metal phosphides (TMPs) have been known as active catalysts for the hydrodesulfurization (HDS) reaction.[11] Insomuch as HDS and HER rely on reversible binding between the catalyst and hydrogen,[12,13] it is expected that TMPs could be active for the HER. Indeed, recent studies demonstrated that some metal phosphides[14−20] and chalcogels[21] can be active

HER electrocatalysts, even though their performance remains inferior to that of Pt/C, pointing toward a possibility for further improvements. Previous reports have revealed that Rh_2P catalyst is highly active for catalyzing the HDS reaction,[22,23] which initiated investigations of its capabilities for the HER. Here we report a Pt-free catalyst based on Rh modified with phosphorus, which had well-defined thin-film surfaces, and corresponding monodisperse rhodium phosphide nanocubes (Rh_2P NCs) supported on high-surface-area carbon. This catalyst exhibits higher HER and OER catalytic activities and better durability than Pt/C and Rh/C catalysts in both acidic and alkaline electrolytes.

RESULTS AND DISCUSSION

Thin-Film Preparation and Analysis. In order to systematically identify and evaluate novel electrocatalytically active systems, it is of paramount importance to construct well-defined surfaces. These systems presumably provide control of critical parameters such as surface area, surface, and subsurface composition and, to some extent, morphology. In our earlier
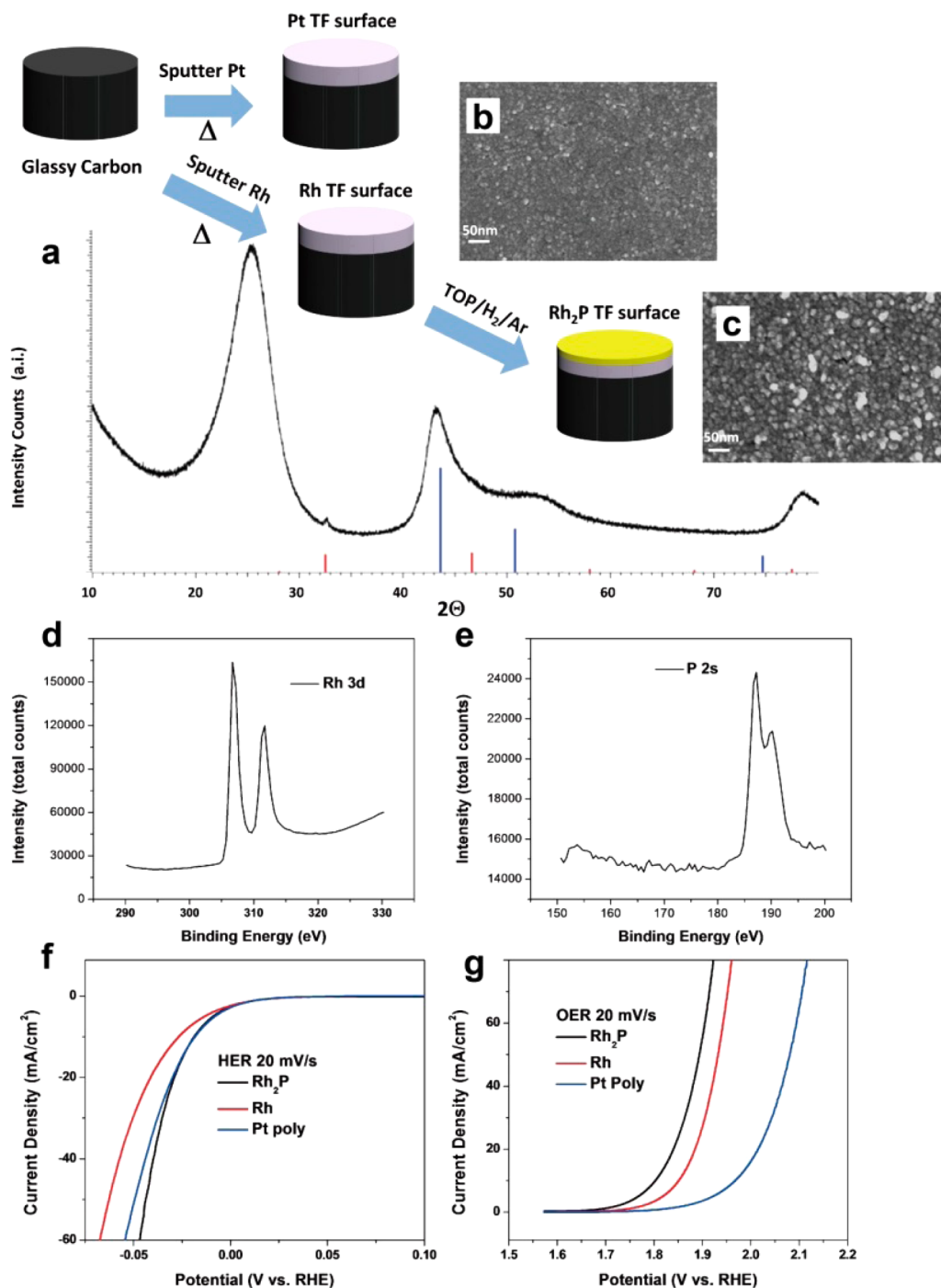
**Figure 1.** Schematic illustration and characterization of Pt, Rh, and Rh$_2$P thin films grown on a glassy carbon substrate. (a) X-ray diffraction of Rh$_2$P thin film, indicating characteristic peaks for both Rh$_2$P (red) and Rh (blue). (b,c) Scanning electron microscopy images of (b) Rh and (c) Rh$_2$P. (d,e) X-ray photoelectron spectroscopy of Rh$_2$P surface, indicating characteristic peaks for (d) rhodium 3d and (e) phosphorus 2s, 187.2 eV (Rh$_2$P) and 190.2 eV (P oxide). (f,g) Polarization curves of Rh$_2$P (black), Rh (red), and Pt (blue) at 20 °C with 20 mV/s at 1600 rpm in 0.5 M H$_2$SO$_4$: (f) HER and (g) OER.

work, we proposed thin-film methodology as a powerful tool in the evaluation of electrochemical systems.[24] Here we applied this approach to investigate the catalytic performance of Pt-free surfaces that are based on Rh and P, which assumed reliance on well-established standards such as Pt surfaces. A magnetron sputtering method was used to deposit Rh thin films over a clean glassy carbon electrode inside an ultra-high-vacuum chamber. Moreover, the Rh thin-film surface was chemically treated in order to induce surface modification by phosphorus,

forming new X-ray diffraction (XRD) peaks which were indexed to the antifluorite structure of Rh$_2$P (card no. 02-1299), as shown in Figure 1. (See Experimental Section and Figures S1 and S2 for detailed thin-film preparation and characterization.) The electrocatalytic performance of Rh and Rh$_2$P thin films with similar surface morphology and geometric surface area is then compared with that of a Pt thin-film electrode (6 mm in diameter). Figure 1 summarizes the thin-film preparation and characterization, including polarization
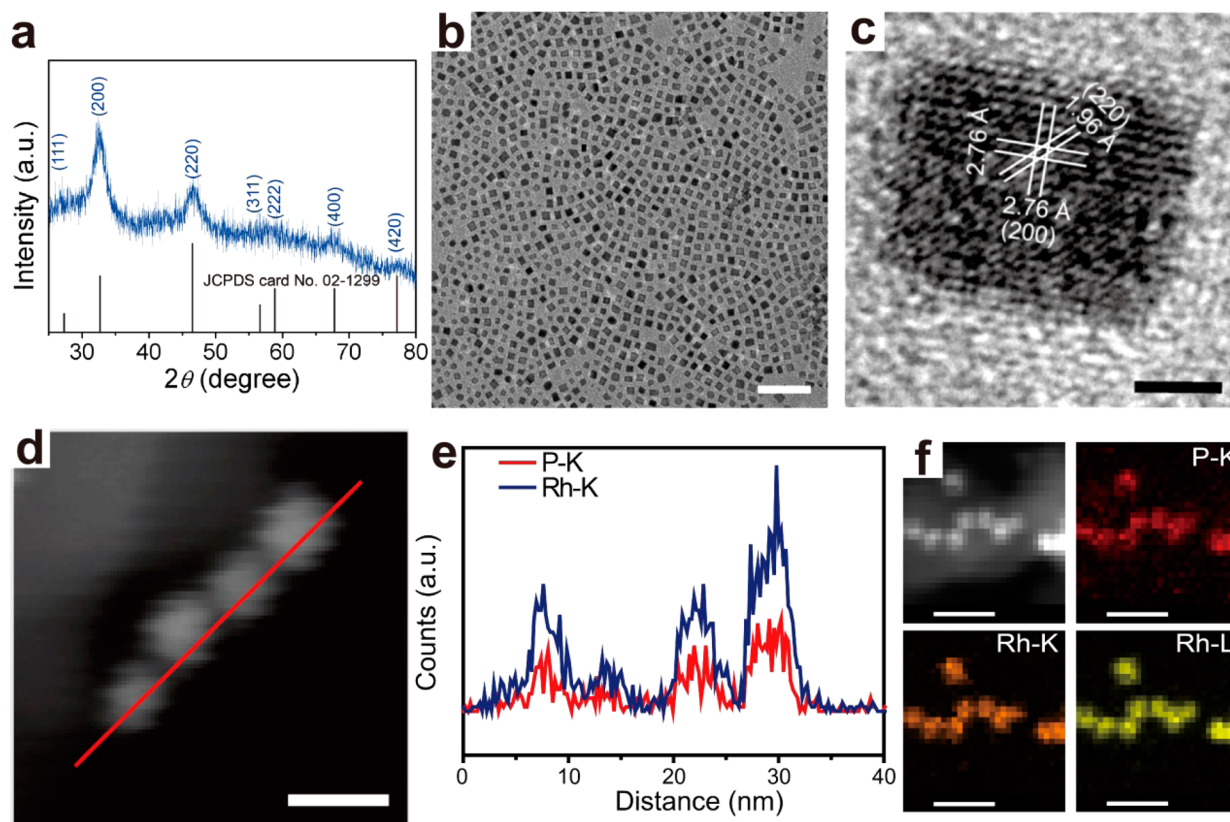
Figure 2. Characterization of rhodium phosphide nanocubes. (a) XRD pattern of the Rh_2P NCs. (b) TEM image of the Rh_2P NCs. Scale bar, 50 nm. (c) HRTEM image of a Rh_2P NC. Scale bar, 2 nm. (d) HAADF-STEM image of Rh_2P NCs with red line showing the line scanning path. Scale bar, 10 nm. (e) Corresponding line-scanning profile. Scale bar, 10 nm. (f) HAADF-STEM image of Rh_2P NCs and corresponding element maps showing the distribution of Rh (orange, yellow) and P (red). Scale bar, 20 nm.

curves for HER and OER in 0.5 M H_2SO_4 for all three surfaces. It turns out that geometrically identical thin-film surfaces with similar surface morphology (see Figure S1) exhibit quite different electrochemical properties. Polarization curves in Figure 1f,g suggest that the order of activity is Rh < Pt < Rh_2P for the HER and Pt < Rh < Rh_2P for the OER. In both cases, surface modification by phosphorus has been found to be crucial in enhancing catalytic performance. These findings were used to design real-world material at nanoscale in the form of Rh_2P nanoparticles dispersed on high-surface-area carbon.

Nanoparticle Synthesis and Structural Characterization. The Rh_2P NCs were synthesized by a one-step solvo-thermal method via a direct reaction between $Rh(acac)_3$ and tri-*n*-octylphosphine (TOP). For comparison, pure Rh and pure Pt NCs were also prepared (see Experimental Section and Figures S3−S5 for details). As shown in Figure 2a, the XRD peaks were indexed to the antifluorite structure of Rh_2P (card no. 02-1299). Transmission electron microscopy (TEM) reveals monodisperse NCs with an average edge length of 4.7 nm (see Figure 2b for TEM image and Figure S3f for size distribution). Figure 2c shows a high-resolution (HR) TEM image of an individual Rh_2P NC along the [100] zone axes. The clear fringes with lattice spacings of 2.76 and 1.96 Å can be indexed to the (200) and (220) planes of the antifluorite structure of Rh_2P, respectively. High-angle annular dark-field scanning transmission electron microscopy−energy-dispersive X-ray spectroscopy (HAADF-STEM-EDS) line scan and mapping analysis confirmed the homogeneous distributions of Rh and P throughout the whole cube (Figure 2d−f). As a

result, we synthesized monodisperse NCs of Pt, Rh, and Rh_2P to keep constant particle size distribution and surface morphology, while the surface composition of Rh particles was controlled by chemical modification by phosphorus. Such an approach allows systematic evaluation of electrochemical properties where only one variable of the system, surface composition, is being changed; i.e., particles with similar shape and size and but different surface composition are compared to each other.

Electrochemical Properties of Nanosized Catalysts. The surface cleanliness of acetic acid-treated Rh_2P NCs supported on carbon (Rh_2P/C) is reflected in the cyclic voltammograms (CVs) (Figure 3a) along with the HER performance (Figure 3b−d). The CV of Rh_2P shows a suppressed onset of hydrogen adsorption and early onset of surface oxidation compared with that of Pt. The polarization curves in Figure 3b show increasing HER activities in the order Rh/C < Pt/C < Rh_2P/C, which matches the one established for well-defined thin-film surfaces. It should be noted that accurate Tafel slope and exchange current density are very difficult to obtain for the nanoscale systems. Instead, the overpotential at given current density can be directly measured by the potentiostat to compare electrocatalytic performance,[21] including *iR* (*i* = current, *R* = resistance) drop compensation. For that reason, as mentioned above, the particle size, shape as well as metal loading of different catalysts were controlled to make reliable comparison of their performance. In the case of Rh_2P/ C, the overpotential at the current density of 5 mA/cm² is 5.4 mV, which is lower than those for Pt/C (8.0 mV) and Rh/C
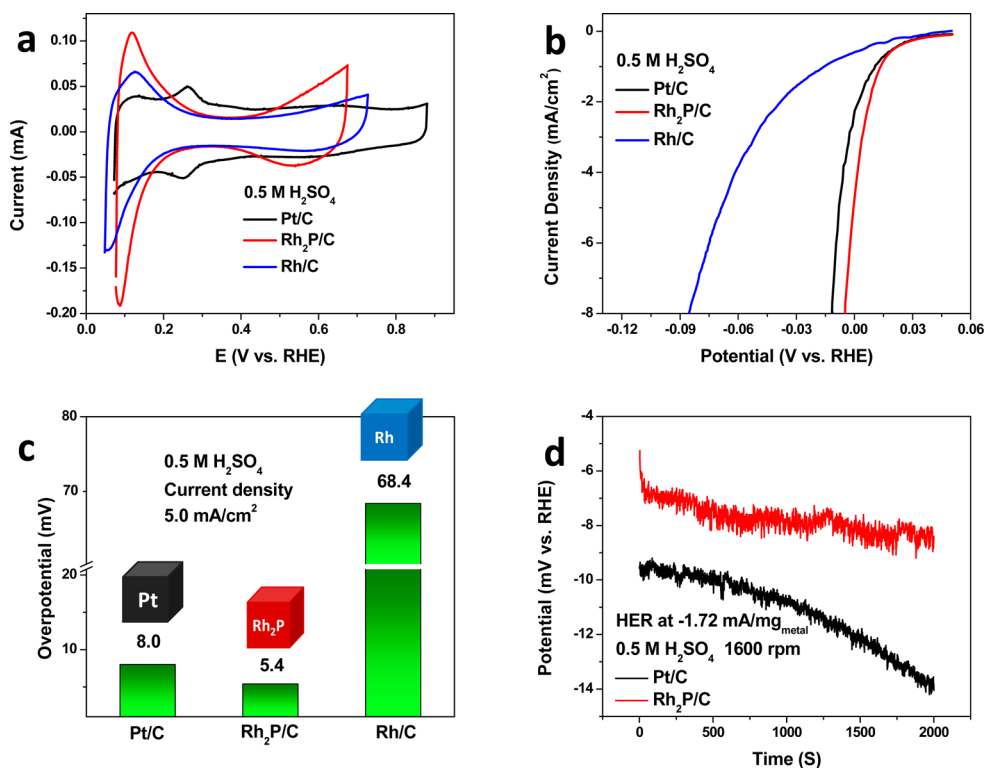
Figure 3. Electrocatalytic properties for the HER in acid (0.5 M H$_2$SO$_4$). (a) Cyclic voltammograms for Pt/C, Rh$_2$P/C, and Rh/C with a scan rate of 50 mV/s. (b) Polarization curves for Pt/C (3.7 μg$_{Pt}$/cm^2), Rh$_2$P/C (3.7 μg$_{Rh}$/cm^2), and Rh/C (13.3 μg$_{Rh}$/cm^2) recorded at 5 mV/s. (c) Corresponding overpotentials at 5.0 mA/cm^2 current density. (d) Chronopotentiometry of the Rh$_2$P/C and Pt/C recorded at −1.72 mA/mg$_{metal}$ current density and room temperature while rotating at 1600 rpm. The potentials were converted to reversible hydrogen electrode (RHE) and corrected for iR drop.
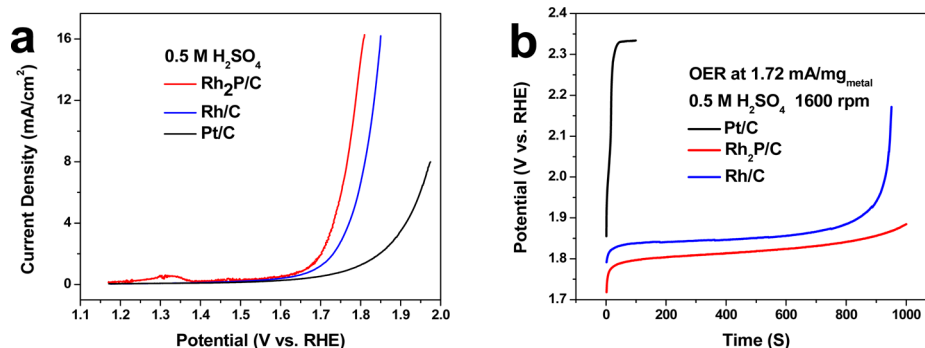

Figure 4. OER activity and stability in acid (0.5 M H$_2$SO$_4$). (a) Polarization curves for Pt/C (3.7 μg$_{Pt}$/cm^2), Rh$_2$P/C (3.7 μg$_{Rh}$/cm^2), and Rh/C (3.7 μg$_{Rh}$/cm^2) recorded at 20 mV/s. (b) Chronopotentiometry of the Rh$_2$P/C, Rh/C, and Pt/C recorded at 1.72 mA/mg$_{metal}$ current density and room temperature while rotating at 1600 rpm. The potentials were converted to RHE and corrected for iR drop.

(68.4 mV) (Figure 3c). The difference between Rh$_2$P/C and Pt/C in terms of HER activity was further revealed by chronopotentiometry. In Figure 3d, at constant current density of −1.72 mA/mg$_{metal}$ (normalized by metal mass loading), the overpotential of Rh$_2$P/C was still lower than that of Pt/C after 2000 s. Therefore, one can conclude that the incorporation of phosphorus greatly enhances the HER activity of Rh$_2$P/C compared to that of pure Rh/C, making it even more active than Pt/C.

In order to illustrate the superior catalytic activity of Rh$_2$P/C, electrochemical impedance spectroscopy (EIS) was performed at an overpotential of η = 3.8 mV. In the Nyquist plot of the EIS response shown in Figure S6, the Rh$_2$P/C exhibits much lower impedance [Faradaic impedance (Z_f), or charge-transfer

impedance, of 2.04 Ω] than the others. Note that the loading amount of Rh in Rh$_2$P/C for catalytic measurement is as low as 3.7 μg/cm^2 determined by ICP-AES (Table S1). These results suggest that superior catalytic performance of Rh$_2$P/C leads to a significant reduction of the precious metal loading that can meet the cost requirements for large-scale applications. Moreover, the Rh$_2$P/C electrocatalyst also performs well in alkaline media, showing higher activity compared with Rh/C and Pt/C (Figure S7).

In addition to the high activity, the Rh$_2$P/C exhibits excellent durability throughout the electrochemical process under strong acidic conditions. The long-term stability of Rh$_2$P/C was evaluated by electrolysis at a fixed overpotential of 109 mV. Figure S8a displays that as much as 93% of the hydrogen
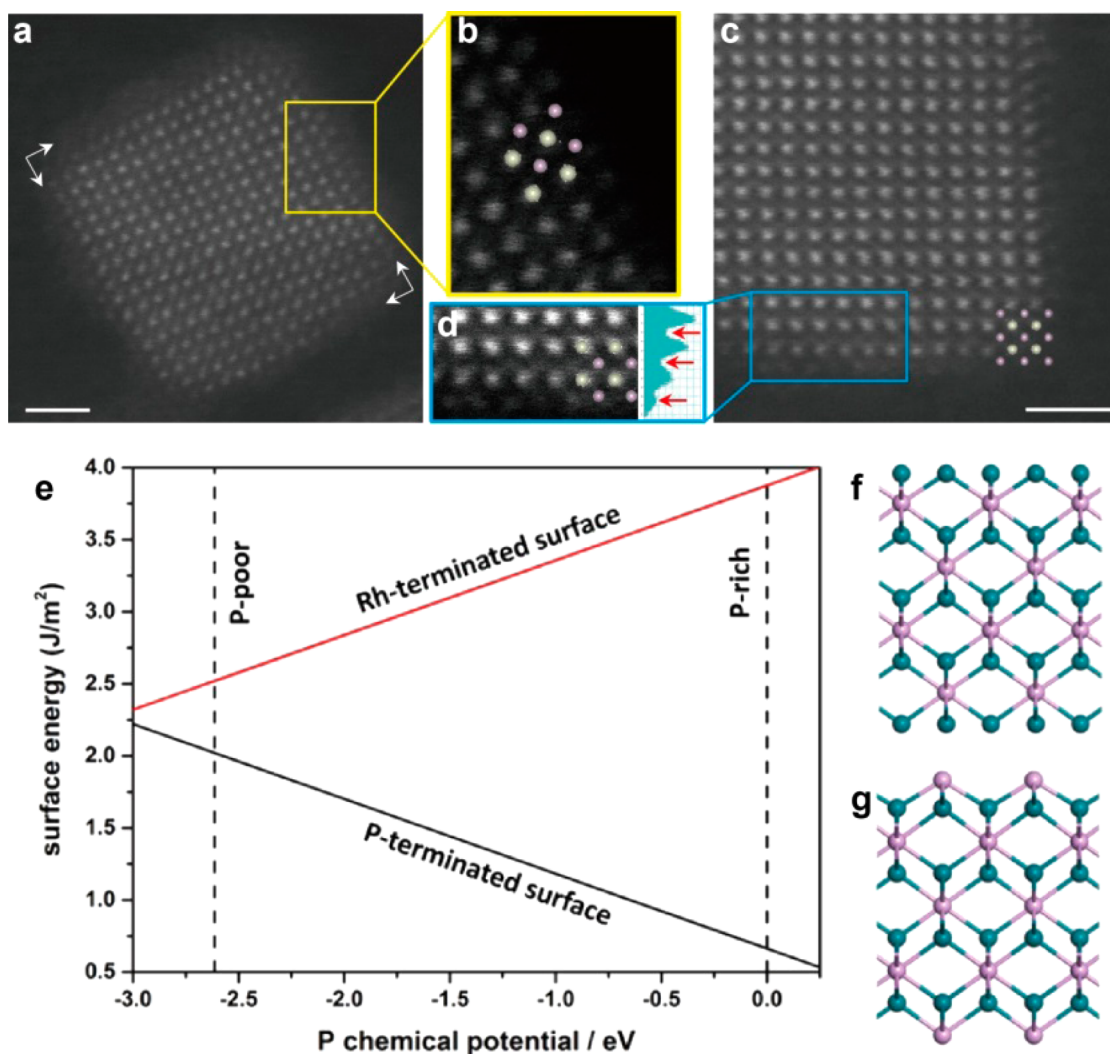
Figure 5. ADF-STEM imaging and calculated surface free energies of the Rh$_2$P NCs. (a,c) ADF-STEM images of two individual Rh$_2$P NCs. Colored frames feature near-surface regions. (b,d) Enlarged images of the frames, showing that the outermost surface is composed of P atoms. Arrows in the intensity profile on the right side of (d) point out the intensity of P columns. Insets in (b−d) display atom model projections along the [001] axis. Scale bars, 1 nm. (e) Calculated surface energies of Rh and P terminations of Rh$_2$P NCs as a function of P chemical potential. The dashed vertical lines indicate the allowed range of the phosphorus chemical potential, using 1/4E (P$_4$, white phosphorus) as zero reference. (f,g) Schematic diagrams of Rh-terminated and P-terminated surfaces, respectively. Cyan spheres indicate Rh atoms, and magenta spheres indicate P atoms.

evolution current density was sustained after 36 000 s. TEM images confirm that the size, morphology, and dispersion of the Rh$_2$P NCs were preserved after 10 h (Figure S8b,c). These results prove that Rh$_2$P/C is stable for long-term hydrogen production from electrolysis of water, making it a promising catalyst in practical application.

The Rh$_2$P/C, Rh/C, and Pt/C catalysts were also tested for OER in 0.5 M sulfuric acid. Figure 4 shows that both the OER activity and stability follow the order of Pt/C < Rh/C < Rh$_2$P/C. From the polarization curves in Figure 4a, at 5 mA/cm^2 current density, Rh$_2$P/C showed 0.51 V overpotential, followed by Rh/C (0.56 V) and Pt/C (0.63 V). It is important to note that catalyst stability for the OER in acidic environment is very challenging. Figure 4b depicts the results obtained by holding at constant current density of 1.72 mA/mg$_{metal}$ (6.38 mA/cm^2 normalized to the geometric surface area of the glassy carbon electrode), both Pt/C and Rh/C did not survive 1000 s of the test, ending up in a sharp spike of potential, which is attributed to the significant metal dissolution. In contrast, the potential of Rh$_2$P/C only increased approximately 0.1 V under the same

conditions. Therefore, it is obvious that as-synthesized Pt and Rh NCs are more vulnerable to metal dissolution than the Rh$_2$P NCs. The OER stability of Rh$_2$P was also tested in 0.1 M perchloric acid by cycling between 1.23 and 1.78 V at 50 mV/s. As summarized in Figure S9, the OER activity slightly increased (7 mV at 5 mA/cm^2) after 100 scans and held until 200 scans. After that, the activity dropped at 300 scans (10 mV at 5 mA/cm^2) compared with initial activity. The amount of Rh found in the electrolyte was 76 ng, which only accounts for 7.2% of the Rh total mass loading (1.05 μg) on the electrode.

Surface Atom Determination. Determination of the near-surface structure and composition is critical in revealing the high performance of Rh$_2$P NC catalyst. For an ideal Rh$_2$P NC with an antifluorite structure and with surface enclosed by facet, the terminated atoms will exclusively be Rh or P. ADF-STEM enabled us to determine the atomic structures[25] of the Rh$_2$P NC. Figure 5a,c shows the ADF-STEM images of two Rh$_2$P NCs oriented along the [001] direction in which the P and Rh atoms are separated in two different columns. Because the contrast approximately scales with $Z^{1.7}$, the brighter columns
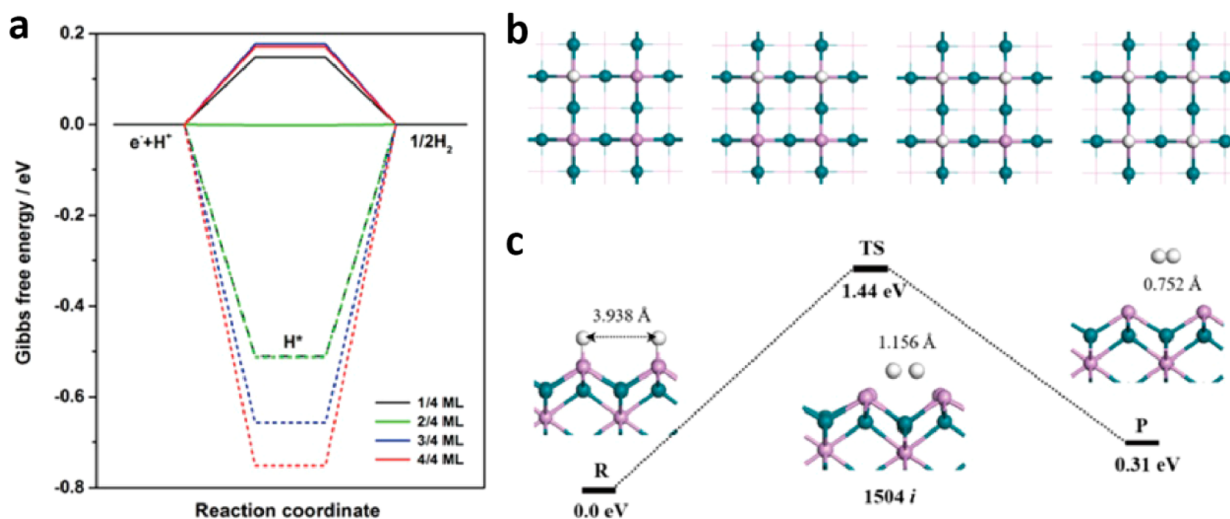
Figure 6. HER mechanism. (a) Gibbs free-energy diagrams for HER on P-terminated (solid line) and Rh-terminated (dashed line) surfaces under different coverage (one, two, three, and four H atoms, considered as 1/4, 2/4, 3/4, and 4/4 monolayer (ML) coverage, respectively). (b) Optimized structures of H adsorption with different coverage on P-terminated surface. (c) Tafel-step reaction pathway of HER on P-terminated surface. Cyan, magenta, and white spheres indicate Rh, P, and H atoms, respectively.

correspond to Rh atoms and the lighter ones correspond to P atoms. Figure 5b,d displays enlarged images of the surfaces, where the outermost atoms locate at P lattice positions and appear lighter than those in the sublayer (also see the intensity profile). This result strongly indicates that the surface atoms can be identified as P atoms. Statistical estimation based on eight Rh$_2$P NCs shows that approximately 67% of the surface atoms are P, suggesting that the outmost atomic layer of Rh$_2$P NCs is P-rich. Figure 5e shows the calculated surface free energies of Rh and P terminations by using periodic density functional theory (DFT). We find that the P-terminated surface (Figure 5g) is more stable than the Rh-terminated surface (Figure 5f) in the whole range of phosphorus chemical potentials from P-rich to P-poor boundaries, indicating that P prefers surface position. This result agrees well with the ADF-STEM observations.

DFT Calculations. Previous studies have proved that the Gibbs free energy of hydrogen adsorption (ΔG°_H) is a reasonable descriptor of HER activity for various catalysts.[26,27] A material will be a good catalyst for hydrogen evolution when ΔG°_H is close to zero, because lower ΔG°_H will lead to the slow hydrogen release step due to the strong bonds with hydrogen atoms, whereas higher ΔG°_H will make the proton/electron-transfer step endothermal. ΔG°_H values of Rh-terminated and P-terminated surfaces with different H coverage were investigated using the DFT method, as shown in Figure 6a and Table S2. The optimized structures of H adsorption are shown in Figure 6b and Figure S10. Rh atoms in the Rh-terminated surface exhibit strong binding to hydrogen atoms under all-hydrogen coverage, which clearly indicates that Rh should not be the active site. However, on P-terminated surface, when hydrogen coverage increases from 25% to 50%, the Gibbs free energy is calculated as 0.00 eV, indicating the vital role of P atoms in hydrogen evolution. To gain more insights into the HER mechanism, we also calculated the combination of two adsorbed hydrogen atoms, i.e., the Tafel step in HER. Figure 6c represents the Tafel step reaction pathway of HER on a P-terminated Rh$_2$P (200) surface. It is found that reactant (R) with two H atoms adsorbed on the two top sites can form product (P) with a weakly absorbed H$_2$ molecule (-0.01 eV)

by crossing the transition state (TS) with H−H distance of 1.156 Å and imaginary vibration frequency of 1504i cm^{-1}. The calculated activation barrier is 1.44 eV (39.1 kcal/mol), suggesting favorable activity for HER.

Our DFT calculations confirm that the high activity of the Rh$_2$P NC for HER arises from P atoms because of the nearly zero Gibbs free energy. To further illustrate the role of P atoms, the electron localization function of Rh$_2$P was calculated, and the results are shown in Figure S11. The calculation results reveal significant covalent interaction between P and Rh and that P atoms are slightly negatively charged. As a result, the binding with H is neither too strong nor too weak, which is consistent with the calculated ΔG°_H. XPS was further carried out to verify the weak electron transfer from Rh to P. Figure S12a,b shows XPS data in the Rh(3d) and P(2p) regions for Rh$_2$P NCs/C sample, respectively. Two peaks are apparent in the Rh(3d) region at 307.7 and 312.2 eV, along with peaks at 130.2 and 131.0 eV in the P(2p) region. The Rh 3d$_{5/2}$ binding energy of 307.7 eV is positively shifted from that of metallic Rh (307.3 eV),[28] suggesting that Rh in Rh$_2$P NCs bears a partial positive charge (δ^+). For the P(2p) region, the peak assigned to the oxidized P species was derived from TOP at around 133.0 eV; the P 2p$_{3/2}$ has a binding energy of 130.2 eV, similar to that of P^0 (130.2 eV),[29] which indicates that P is nearly charge neutral. These results points to weak electron density transfer from Rh to P in the Rh$_2$P NCs. On the other hand, it is conceivable that the phosphorus that dominates the surface of Rh$_2$P NCs will not be stable in the OER potential range in an acidic electrolyte. During OER, the continuous dissolution of P may promote the formation of rhodium oxide from the partially positive Rh. In addition, with the P-rich surface, its dissolution may also increase the surface roughness (i.e., the density of defects/under-coordinated atoms) of the catalyst, giving rise to the enhanced OER activity compared with Rh NPs.[30]

Indeed, our DFT calculations confirm that the P-defect can be formed easily (formation energy $E_f = 2.80$ eV in a P-rich condition), and this surface defect will play a vital role in OER activity. The free-energy profiles of the OER process are illustrated in Figure S13, and the calculation data are listed in Table S3, where $U = 1.74$ V (i.e., an overpotential of 0.51 V) is

determined via experiment. The optimized structures of the intermediates in OER on Rh_2P (200) surface with one defect are shown in Figure S14. On the Rh_2P (200) defect surface, the first adsorbed H_2O binds one proton to form *OH (structure b) spontaneously due to the downhill free-energy profile of 1.12 eV. Meanwhile, another H_2O molecule adsorbed on another Rh−Rh bridge site can immediately obtain an electron, leading to the second *OH (structure c). This step is calculated to be exothermic by 0.89 eV. As the reaction continues, two *OH lose one proton in quick succession (structures d and e), and the ΔG goes further downhill. The third water molecule adsorbs and transfers one proton, resulting in the formation of *OOH (structure f). The similar process also occurs on another *O (structure g). These steps are calculated to be endothermic by 0.13 and 0.47 eV, respectively. Finally, two electrons are captured consecutively, leading to two desorbed O_2 molecules (structures h and i) and a presumptive defect surface (structure a). Therefore, the overall energy barrier on the Rh_2P (200) defect surface is 0.60 eV after the continuous uphill steps of fifth and sixth proton removal, which suggests that the 0.51 V overpotential can drive the OER on this surface. To further illustrate the role of defect, the OER on perfect Rh_2P NCs has also been investigated. The calculation results show that the largest free-energy difference is 1.71 eV, corresponding to splitting the third proton to form *OOH. It follows that OER cannot occur on Rh_2P surface without defect unless we increase the overpotential. The calculation details on Rh_2P surface without defect are shown in Figures S15 and S16, and Table S4. Based on the DFT calculations, the poor property for OER on Rh_2P surface without defect is attributed to the strong binding with *O and weak binding with *OOH, which leads to the enormous ΔG in the third step. The presence of surface defect can balance the binding intensity between *OOH and *O, leading to the decreasing free-energy barrier and the enhanced OER activity.

CONCLUSION

Our studies have revealed that Rh_2P NCs with P-rich surface exhibit extraordinary catalytic performance for HER in acid, which exceeds the activity of pure Pt catalyst. The Rh_2P NCs also show enhanced OER activity and stability compared with as-synthesized Rh/C and Pt/C catalysts with the help of surface defects. Further investigation on the reaction mechanism as well as fine-tuning the surface structure can help to design more favorable catalysts that are both low-cost and precious-metals-free.

EXPERIMENTAL SECTION

Reagents. The synthesis was carried out using a solvothermal method with commercial reagents. Rhodium(III) acetylacetonate [Rh(acac)$_3$, 99%], rhodium(III) chloride hydrate (RhCl$_3$·xH$_2$O), tri-n-octylphosphine (TOP), and trimethyl(tetradecyl)ammonium bromide (TTAB) were purchased from Alfa Aesar. Benzyl ether and oleylamine (OAm) were purchased from Acros. Poly-(vinylpyrrolidone) (PVP, M_w = 24 000), acetic acid, ethanol, cyclohexane, and ethylene glycol were purchased from Sinopharm Chemical Reagent Co. Ltd. (Shanghai, China). Iron pentacarbonyl [Fe(CO)$_5$], oleic acid (OAc), Nafion-117 (5%), and potassium hydroxide (99.99% trace metal basis) were purchased from Sigma-Aldrich. Platinum acetylacetonate [Pt(acac)$_2$, 98%] was from STREM Chemical. Sulfuric acid and perchloric acid were produced by EMD. All reagents were used as received without further purification.

Thin-Film Preparation. Rh thin films of 20 nm thickness were deposited onto polished glassy carbon disks (6 mm in diameter, 4 mm

in height) by magnetron sputtering (AJA International, Inc.) at 0.98 Å/s.[31] The as-sputtered thin films were annealed at 400 °C for 1 h in the same chamber under ultra-high-vacuum condition (∼10⁻⁹ Torr) to smooth the surface. Rh_2P thin-film growth was modified from literature.[32] The carbon disks with 20 nm Rh were placed in a crucible in the center of a tube furnace under flow of forming gas (4% H_2 in Ar). Another crucible with 5 mL of TOP was placed near the gas inlet inside the same tube furnace. The furnace was gradually heated to 400 °C, kept for 30 min, and then cooled down to room temperature. The disks were rinsed with ethanol. The disks were subsequently placed in a clean crucible inside a clean tube furnace without TOP and annealed at 450 °C for 30 min.

Synthesis of Rh_2P Nanocubes. The Rh_2P NCs were synthesized using a solvo-thermal method. In a typical procedure, 0.01 mmol of Rh(acac)$_3$ and 30 μL (0.067 mmol) of TOP were added to 5 mL of OAm. The mixture was stirred vigorously at room temperature for 10 min and then transferred to a Teflon-lined stainless steel autoclave. The autoclave was sealed and maintained at 180 °C for 12 h, and then cooled down to room temperature. The resulting black product was precipitated with ethanol (20 mL), separated by centrifugation with rate 10000 rpm for 10 min, and washed three times by precipitation/dissolution with ethanol/cyclohexane.

Synthesis of Rh Nanocubes. The synthesis of Rh NCs was carried out using a modified reported method.[33] In the present work, the amount of TTAB was twice of that of reported one while other experimental conditions were kept the same. The TEM image and corresponding XRD pattern are shown in Figures S3 and S4, respectively.

Synthesis of Pt Nanocubes. First, 0.10 g of Pt(acac)$_2$, 1 mL of OAc, 6 mL of OAm, and 10 mL of benzyl ether were mixed in a flask and stirred at 300 rpm under argon flow. The mixture was then heated to 110 °C, kept for 10 min, and further heated to 170 °C. In the meantime, Fe(CO)$_5$ was diluted in chloroform to make 10% (volume percentage) Fe(CO)$_5$ solution. Next, 0.25 mL of this 10% Fe(CO)$_5$ solution was injected to the flask at 170 °C. After that, the temperature was increased to 210 °C and kept for 1 h. The Pt NCs were precipitated out by ethanol, centrifuged at 8000 rpm for 5 min, and then collected in hexane.

Preparation of Electrocatalysts. In order to increase the stability as well as the conductivity, carbon black (Cabot, Vulcan XC-72) was used as the catalyst support.[10] Specifically, the as-synthesized Rh_2P and Rh NCs were dispersed in cyclohexane and incorporated onto carbon black. The obtained samples were refluxed in acetic acid at 70 °C for 12 h;[34] they were further washed with ethanol and dried in a vacuum at 60 °C for 12 h. The Pt NCs were loaded on the same type of carbon support in chloroform and sonicated for 1 h. The catalyst was then dried and heated at 185 °C in air for 12 h to remove the surfactant.

Preparation of Working Electrodes. Catalyst solutions of Rh_2P/C and Rh/C dispersed in water/isopropanol (v:v = 3:1) solution with catalyst concentrations of 0.7 mg/mL (Rh_2P) and 2 mg/mL (Rh) were prepared by sonication, respectively. The catalyst inks of the above solutions were then loaded onto a glassy carbon electrode of 0.283 cm² geometric surface. The metal loading was 3.7 μg$_{Rh}$/cm² for Rh_2P/C. For Rh/C, the loading was 13.3 μg$_{Rh}$/cm² (HER) or 3.7 μg$_{Rh}$/cm² (OER). A 0.5 mg/mL ink of Pt/C was also prepared using Milli-Q water. The metal mass loading of Pt was controlled to be higher than that of the Rh_2P/C (5.0 μg$_{Pt}$/cm²), because of its larger size. A 10 μL solution of 0.1% Nafion was added onto each catalyst electrode to keep it from falling during electrochemical measurement.

Electrochemical Measurements. All the electrochemical measurements were performed using an Autolab 302 potentiostat. All measurements were obtained at room temperature using a typical three-compartment cell that included a Ag/AgCl electrode as the reference electrode and a Au wire as the counter electrode. The counter electrode was separated from the main chamber of the working electrode via a fritted glass to avoid possible Au deposition on the working electrode. The electrolyte used was 0.5 M sulfuric acid (H_2SO_4), 0.1 M perchloric acid ($HClO_4$), or 0.1 M potassium hydroxide (KOH). For alkaline experiment, Pt/C was first cycled in 0.1 M $HClO_4$ for 10 scans between 0.06 and 0.97 V, 50 mV/s, to

remove the surface iron oxide. Electrochemical impedance spectroscopy (EIS) measurements were performed in the frequency range from 100 kHz to 100 mHz. The electrochemical stability of the catalysts were tested by potentiostatically maintaining them under constant voltage, $\eta = 109$ mV, at room temperature for 10 h. All the potentials reported in this work were converted to the reversible hydrogen electrode (RHE).

Instrumentation. Samples for X-ray diffraction (XRD) analysis were prepared by drying a few drops of concentrated colloid dispersion of Rh_2P or other products in cyclohexane on glass. XRD patterns were recorded with a Rigaku RU-200b X-ray powder diffractometer with Cu Kα radiation ($\lambda = 1.5406$ Å). Particles sizes and morphologies were determined by using a Hitachi H-800 transmission electron microscope (TEM) and a FEI Tecnai G2 F20 S-Twin high-resolution transmission electron microscope (HRTEM) operated at 200 kV. The Rh_2P NCs were imaged with annular dark-field scanning transmission electron microscopy (ADF-STEM). The ADF-STEM images were captured with a Titan 80-300 scanning transmission electron microscope operated at 300 kV, equipped with a probe spherical aberration corrector. The relative small collection angle (15−88 mrad) increases the intensity from low Z number atoms such as P. Thin-film surface morphologies were characterized by using a Hitachi S4700-II scanning electron microscope (SEM). X-ray photoelectron spectroscopy (XPS) analysis was carried out on an ULVAC PHI Quantera microprobe using Al Kα as the source type, spot size of 500 μm, pass energy of 30.0 eV, and energy step size of 0.050 eV.

COMPUTATIONAL METHODS AND MODELS

All the calculations were performed by using periodic density functional theory (DFT) with the Vienna Ab-initio Simulation Package (VASP).[35,36] The projector augmented wave (PAW) method was used to describe the interaction between the atomic cores and electrons with a kinetic cutoff of 400 eV.[37] We applied the generalized gradient approximation (GGA) with the Perdew−Burke−Ernzerhof (PBE) exchange-correlation functional.[38] The Rh_2P (200) surfaces of two possible terminations were modeled by a nonstoichiometric 2×2 eight-atom-layer supercell slab to eliminate the polarity, with a vacuum gap of ~15 Å. A Monkhorst−Pack grid of size of 3×3×1 was used to sample the surface Brillouin zone. The lowest two layers were fixed, and the other atoms were fully optimized until the residual force on each ion was less than 0.02 eV/Å. The standard dimer method was used to search for the transition states.[39]

Surface Free Energy and Defect Formation Energy. The surface free energy γ can be calculated using the equation[40]

$$\gamma = (G_{slab} - N_{Rh}\mu_{Rh} - N_P\mu_P)/2A$$
$$= [G_{slab} - N_{Rh}g_{bulk}/2 + (N_{Rh}/2 - N_P)\mu_P]/2A$$

where A is the area of the surface unit cell, g_{bulk} is the Gibbs free energy per formula unit in Rh_2P bulk, N_{Rh} and N_P are the numbers of Rh and P atoms in the three-dimensional supercell, and μ_{Rh} and μ_P are the chemical potentials of a Rh atom and a P atom, respectively. The range of μ_P can be estimated as follows:

$$\min(\mu_P) = g_{bulk}(Rh_2P) - 2g_{bulk}(Rh)$$

$$\max(\mu_P) = \frac{1}{4}E(P_4, \text{ white phosphorus})$$

where $g_{bulk}(Rh)$ is the Gibbs free energy per formula unit in Rh bulk and $E(P_4$, white phosphorus) is the total energy of a free, isolated P_4 molecule at $T = 0$ K.

The defect formation energy can be calculated with the equation

$$E_f = E(Rh_2P\text{-defect}) + \frac{1}{4}E(P_4) - E(Rh_2P)$$

where $E(Rh_2P\text{-defect})$, $E(Rh_2P)$, and $E(P)$ represent the energies of Rh_2P with a defect, Rh_2P, and P_4 molecule, respectively.

Hydrogen Adsorption and Free Energy. The differential adsorption energy ΔE_H can be estimated by using the equation

$$\Delta E_H = E(Rh_2P + nH) - E(Rh_2P + (n-1)H) - \frac{1}{2}E(H_2)$$

where $E(Rh_2P + nH)$, $E(Rh_2P + (n-1)H)$, and $E(H_2)$ represent the total energy of Rh_2P with n hydrogen atoms adsorbed on surface, the total energy of Rh_2P with $(n-1)$ hydrogen atoms adsorbed on surface, and the total energy of a hydrogen molecule in the gas phase, respectively. Top (T), bridge (B), and hollow (H) sites were considered for the adsorption of a H atom on both P-terminated and Rh-terminated surfaces (see Figure S17). The results (see Table S5) show that the top site is favorable for H adsorption on the P-terminated surface, while the favorable binding site on the Rh-terminated surface is the hollow2 site.

The Gibbs free energy of hydrogen adsorption ΔG°_H can be calculated with the equation

$$\Delta G^\circ_H = \Delta E_H + \Delta E_{ZPE} + \Delta_{0 \to 298K}\Delta H_H - T\Delta S_H$$

where ΔE_{ZPE}, $\Delta_{0 \to 298K}\Delta H_H$, and ΔS_H are the differences in zero point energy (ZPE), in enthalpy change from 0 to 298 K, and in entropy between the adsorbed state and the gas phase, respectively. Considering that the vibrational entropy of H* in the adsorbed state is small, we can take the entropy of hydrogen adsorption as $\Delta S_H = \frac{1}{2}S^\circ_{H_2}$, where $S^\circ_{H_2}$ is the entropy of H_2 in the gas phase at standard conditions. Likewise, $\Delta_{0 \to 298K}\Delta H_H$ is equal to half of $\Delta_{0 \to 298K}\Delta H_{H_2}$.

Free-Energy Profile in OER. To derive the free-energy reaction profile, we first obtain the enthalpy energy of each elementary step (ΔH at 0 K, 0 bar), which approximately equals to the DFT total energy (ΔE) after ZPE correction (ΔE_{ZPE}). For adsorbed species, ΔH at 0 K, 0 bar is a good approximation to the Gibbs free energy (ΔG), as the entropy (S) contributions are small. However, for gaseous or liquid molecules, such as oxygen, hydrogen, and water, the large entropy term at elevated temperatures cannot be neglected. Therefore, G of H_2O and H_2 can be estimated by the equation

$$G = E + E_{ZPE} + \Delta H_{(0 \to 298K)} - TS$$

where E_{ZPE}, $\Delta H_{(0 \to 298K)}$, and S are the ZPE correction, enthalpy difference between 0 and 298 K, and entropy, respectively.

The G value of O_2 (shown as $G[O_2]$) can be calculated with the following equation according to the OER equilibrium at the standard conditions:

$$G[O_2] = 4.92 \text{ eV} + 2G[H_2O] - 2G[H_2]$$

Next, we must consider the proton when calculating the Gibbs free-energy change (ΔG) of an elementary step. It is well known that, at pH = 0 in the electrolyte and 1 bar of H_2 in the gas phase at 298 K, the reaction free energy of $\frac{1}{2}H_2 \to H^+ + e^-$ equals to zero at an electrode potential of $U = 0$. Therefore, at standard conditions ($U = 0$, pH = 0, p = 1 bar, T = 298 K), ΔG of the reaction $*AH \to A + H^+ + e^-$ is equal to ΔG of the reaction $*AH \to A + \frac{1}{2}H_2$. Finally, the effect of a bias on all states involving an electron in the electrode should be corrected by shifting the energy of this state by $\Delta G_U = -eU$, where U is the electrode potential relative to the standard hydrogen electrode.

ASSOCIATED CONTENT

Ⓢ Supporting Information

The Supporting Information is available free of charge on the ACS Publications website at DOI: 10.1021/jacs.7b01376.

> Figures S1−S17 and Tables S1−S5, showing sample characterizations (SEM, TEM, XPS, XRD), Nyquist plots, HER reaction properties in alkaline media, durability performance, OER stability under potential cycling, and DFT data (PDF)

■ AUTHOR INFORMATION

Corresponding Authors

*junli@tsinghua.edu.cn
*vrstamenkovic@anl.gov
*ydli@mail.tsinghua.edu.cn

ORCID ⦿

Haohong Duan: 0000-0002-9241-0984

Jun Li: 0000-0002-8456-3980

Yadong Li: 0000-0003-1544-1127

Author Contributions

∇H.D., D.L., and Y.T. contributed equally.

Notes

The authors declare no competing financial interest.

■ REFERENCES

(1) Dresselhaus, M. S.; Thomas, I. L. *Nature* **2001**, *414*, 332.
(2) Turner, J. A. *Science* **2004**, *305*, 972.
(3) Gray, H. B. *Nat. Chem.* **2009**, *1*, 7.
(4) Walter, M. G.; Warren, E. L.; McKone, J. R.; Boettcher, S. W.; Mi, Q. X.; Santori, E. A.; Lewis, N. S. *Chem. Rev.* **2010**, *110*, 6446.
(5) Markovic, N. M.; Ross, P. N., Jr. *Surf. Sci. Rep.* **2002**, *45*, 117.
(6) Sheng, W. C.; Gasteiger, H. A.; Shao-Horn, Y. *J. Electrochem. Soc.* **2010**, *157*, B1529.
(7) Schuldiner, S. *J. Electrochem. Soc.* **1959**, *106*, 891.
(8) Morales-Guio, C. G.; Stern, L. A.; Hu, X. *Chem. Soc. Rev.* **2014**, *43*, 6555.
(9) Subbaraman, R.; Tripkovic, D.; Chang, K. C.; Strmcnik, D.; Paulikas, A. P.; Hirunsit, P.; Chan, M.; Greeley, J.; Stamenkovic, V.; Markovic, N. M. *Nat. Mater.* **2012**, *11*, 550.
(10) Chen, C.; Kang, Y. J.; Huo, Z. Y.; Zhu, Z. W.; Huang, W. Y.; Xin, H. L.; Snyder, J. D.; Li, D. G.; Herron, J. A.; Mavrikakis, M.; Chi, M. F.; More, K. L.; Li, Y. D.; Markovic, N. M.; Somorjai, G. A.; Yang, P. D.; Stamenkovic, V. R. *Science* **2014**, *343*, 1339.
(11) Carenco, S.; Portehault, D.; Boissiere, C.; Mezailles, N.; Sanchez, C. *Chem. Rev.* **2013**, *113*, 7981.
(12) Liu, P.; Rodriguez, J. A.; Asakura, T.; Gomes, J.; Nakamura, K. *J. Phys. Chem. B* **2005**, *109*, 4575.
(13) Liu, P.; Rodriguez, J. A. *J. Am. Chem. Soc.* **2005**, *127*, 14871.
(14) Popczun, E. J.; McKone, J. R.; Read, C. G.; Biacchi, A. J.; Wiltrout, A. M.; Lewis, N. S.; Schaak, R. E. *J. Am. Chem. Soc.* **2013**, *135*, 9267.
(15) Xing, Z.; Liu, Q.; Asiri, A. M.; Sun, X. *Adv. Mater.* **2014**, *26*, 5702.
(16) Tian, J.; Liu, Q.; Cheng, N.; Asiri, A. M.; Sun, X. *Angew. Chem., Int. Ed.* **2014**, *53*, 9577.
(17) Liu, Q.; Tian, J.; Cui, W.; Jiang, P.; Cheng, N.; Asiri, A. M.; Sun, X. *Angew. Chem., Int. Ed.* **2014**, *53*, 6710.
(18) Wang, X.; Kolen'ko, Y. V.; Bao, X. Q.; Kovnir, K.; Liu, L. *Angew. Chem., Int. Ed.* **2015**, *54*, 8188.
(19) Wang, C.; Hu, F.; Yang, H.; Zhang, Y.; Lu, H.; Wang, Q. *Nano Res.* **2017**, *10*, 238.
(20) Huang, J.; Li, Y.; Xia, Y.; Zhu, J.; Yi, Q.; Wang, H.; Xiong, J.; Sun, Y.; Zou, G. *Nano Res.* **2017**, *10*, 1010.
(21) Staszak-Jirkovsky, J.; Malliakas, C. D.; Lopes, P. P.; Danilovic, N.; Kota, S. S.; Chang, K. C.; Genorio, B.; Strmcnik, D.; Stamenkovic, V. R.; Kanatzidis, M. G.; Markovic, N. M. *Nat. Mater.* **2016**, *15*, 197.
(22) Hayes, J. R.; Bowker, R. H.; Gaudette, A. F.; Smith, M. C.; Moak, C. E.; Nam, C. Y.; Pratum, T. K.; Bussell, M. E. *J. Catal.* **2010**, *276*, 249.
(23) Kanda, Y.; Temma, C.; Nakata, K.; Kobayashi, T.; Sugioka, M.; Uemichi, Y. *Appl. Catal., A* **2010**, *386*, 171.
(24) van der Vliet, D. F.; Wang, C.; Tripkovic, D.; Strmcnik, D.; Zhang, X. F.; Debe, M. K.; Atanasoski, R. T.; Markovic, N. M.; Stamenkovic, V. R. *Nat. Mater.* **2012**, *11*, 1051.
(25) Xin, H. L.; Alayoglu, S.; Tao, R.; Genc, A.; Wang, C. M.; Kovarik, L.; Stach, E. A.; Wang, L. W.; Salmeron, M.; Somorjai, G. A.; Zheng, H. *Nano Lett.* **2014**, *14*, 3203.
(26) Hinnemann, H.; Moses, P. G.; Bonde, J.; Jørgensen, K. P.; Nielsen, J. H.; Horch, S.; Chorkendorff, I.; Norskov, J. K. *J. Am. Chem. Soc.* **2005**, *127*, 5308.
(27) Skulason, E.; Tripkovic, V.; Bjorketun, M. E.; Gudmundsdottir, S.; Karlberg, G.; Rossmeisl, J.; Bligaard, T.; Jonsson, H.; Nørskov, J. K. *J. Phys. Chem. C* **2010**, *114*, 18182.
(28) Tolia, A. A.; Smiley, R. J.; Delgass, W. N.; Takoudis, C. G.; Weaver, M. J. *J. Catal.* **1994**, *150*, 56.
(29) Seah, M. P.; Briggs, D. *Practical Surface Analysis, Auger and X-ray Photoelectron Spectroscopy*; Wiley & Sons, UK, 1990.
(30) Danilovic, N.; Subbaraman, R.; Chang, K. C.; Chang, S. H.; Kang, Y.; Snyder, J.; Paulikas, A. P.; Strmcnik, D.; Kim, Y. T.; Myers, D.; Stamenkovic, V. R.; Markovic, N. M. *Angew. Chem., Int. Ed.* **2014**, *53*, 14016.
(31) Snyder, J.; Danilovic, N.; Paulikas, A. P.; Tripkovic, D.; Strmcnik, D.; Markovic, N. M.; Stamenkovic, V. R. *J. Phys. Chem. C* **2013**, *117*, 23790.
(32) Read, C. G.; Callejas, J. F.; Holder, C. F.; Schaak, R. E. *ACS Appl. Mater. Interfaces* **2016**, *8*, 12798.
(33) Zhang, Y. W.; Grass, M. E.; Kuhn, J. N.; Tao, F.; Habas, S. E.; Huang, W. Y.; Yang, P. D.; Somorjai, G. A. *J. Am. Chem. Soc.* **2008**, *130*, 5868.
(34) Mazumder, V.; Sun, S. *J. Am. Chem. Soc.* **2009**, *131*, 4588.
(35) Kresse, G.; Furthmüller, J. *Phys. Rev. B: Condens. Matter Mater. Phys.* **1996**, *54*, 11169.
(36) Kresse, G.; Furthmüller, J. *Comput. Mater. Sci.* **1996**, *6*, 15.
(37) Kresse, G.; Joubert, D. *Phys. Rev. B: Condens. Matter Mater. Phys.* **1999**, *59*, 1758.
(38) Perdew, J. P.; Burke, K.; Ernzerhof, M. *Phys. Rev. Lett.* **1996**, *77*, 3865.
(39) Henkelman, G.; Jonsson, H. *J. Chem. Phys.* **1999**, *111*, 7010.
(40) Reuter, K.; Scheffler, M. *Phys. Rev. B: Condens. Matter Mater. Phys.* **2001**, *65*, 035406.